ESI

A tandem nanoreactor constructed by coating Cu_2O on the surface of single-atom catalyst Ni-NC_3 for electroreduction of CO_2 to C_2 products

Cheng-Peng Liang[a], Jia-Run Huang[a], Pei-Qin Liao*[a] and Xiao-Ming Chen*[a,b]

MOE Key Laboratory of Bioinorganic and Synthetic Chemistry, GBRCE for Functional Molecular Engineering, School of Chemistry, IGCME, Sun Yat-Sen University, Guangzhou 510275, China.
Chemistry and Chemical Engineering Guangdong Laboratory, Shantou 515021, China.
E-mail: liaopq3@mail.sysu.edu.cn; cxm@mail.sysu.edu.cn

Experiment Section.

Figure S1. PXRD patterns of **MAF-5**.

Figure S2. PXRD pattern of **Ni-NC$_3$**.

Figure S3. PXRD patterns of **Ni-NC$_3$@Cu$_2$O-30**, **Ni-NC$_3$@Cu$_2$O-10, Carbon Paper@Cu$_2$O** and **Blank Carbon Paper**.

Figure S4. Ni *K*-edge XANES spectra of **Ni-NC$_3$@Cu$_2$O-10** and Ni-based references.

Figure S5. Ni *K*-edge EXAFS spectra of **Ni-NC$_3$@Cu$_2$O-10** and Ni-based references.

Figure S6. The *R*′ space fitting of the coordination structure of nickel ions in **Ni-NC$_3$**.

Figure S7. XPS spectra of **Ni-NC$_3$@Cu$_2$O-10**.

Figure S8. XPS spectra of **Ni-NC$_3$@Cu$_2$O-30**.

Figure S9. Size distribution of **Ni−NC$_3$@Cu$_2$O-10**.

Figure S10. SEM and EDX elemental mapping images of **Ni-NC$_3$@Cu$_2$O-10**.

Figure S11. Energy-dispersive X-ray (EDX) spectrum of **Ni−NC$_3$@Cu$_2$O-10**.

Figure S12. SEM and EDX elemental mapping images of **Ni-NC$_3$@Cu$_2$O-30**.

Figure S13. Energy-dispersive X-ray (EDX) spectrum of **Ni−NC$_3$@Cu$_2$O-30**.

Figure S14. GC profiles of gas products of **Ni−NC$_3$@Cu$_2$O-10** at different potentials.

Figure S15. ^{1}H NMR spectra of the liquid products by using **Ni−NC$_3$@Cu$_2$O-10** as catalyst at different potentials.

Figure S16. FE values of reduced products by **Ni-NC$_3$@Cu$_2$O-10** and **Ni-NC$_3$@Cu$_2$O-30,** respectively.

Figure S17. *i-t* curves by **Ni-NC$_3$@Cu$_2$O-10** at different potentials.

Figure S18. Performance comparison of reported copper-based tandem catalysts for eCO_2RR to C_2 products.

Figure S19. Anodic stripping voltammograms of **Ni-NC$_3$**.

Figure S20. PXRD patterns of **MAF-4**.

Figure S21. SEM images of **Ni-N$_4$@Cu$_2$O-10** and **CB@Cu$_2$O-10**.

Figure S22. LSV curves by **Cu$_2$O** and **Cu$_2$O/Ni-NC$_3$**, respectively, in CO_2-saturated 1 M KOH solution.

Experiment Section.

Materials and Methods. All reagents were commercially available and used without further purification. **MAF−5** and **MAF−4** were synthesized according to the literature.[1, 2] Powder X-ray diffraction (PXRD) patterns were collected on a Bruker D8-Advance diffractometer with Cu *K*α radiation and a LynxEye detector. X-ray photoelectron spectroscopy (XPS) measurements were performed with a VG Scientific ESCALAB 250 instrument. Scanning electron microscope (SEM) images were obtained from an Ultra-high resolution electron microscope (FE-SEM, SU8010). The content of Ni and Cu in electrolyte was detected by inductively coupled plasma atomic emission spectroscopy (ICP-AES) on an IRIS(HR) analyzer.

Attenuated total reflectance Fourier transform infrared spectroscopy (ATR-FTIR) measurements: ATR-FTIR measurements were carried out on a Thermo Scientific Nicolet iS50 (Thermo Fisher) device. The Ge ATR crystal is placed in a three-electrode spectroelectrochemical cell. During ATR-FTIR measurements, Pt wire served as the counter electrode and the Ag/AgCl electrode served as the reference electrode. Under the condition of -1.4 V vs RHE and 1 M KOH aqueous solution, the eCO_2RR data of the same sample were collected after being purified by high-purity CO_2 gas for 30 min. And the IR data from 0 to 20 min were recorded. The collected background has been subtracted in all infrared spectra.

Cu and Ni *K*-edge X-ray absorption fine structure (XAFS) spectroscopy was carried out using the Rapid XAFS 1M (Anhui Absorption Spectroscopy Analysis Instrument Co., Ltd.) by transmission mode at 20 kV and 40 mA, the Si(551) spherically bent crystal analyzer with a radius of curvature of 500 mm was used for Ni, and the data were collected using solid-state detector under ambient condition. The beam size was limited by the horizontal and vertical slits with the area of 1 × 4 mm^2 during XAS measurements.

To obtain the quantitative structural parameters around central atoms, least squares curve parameter fitting was performed using the ARTEMIS module of IFEFFIT software packages. The following EXAFS equation was used:

$$\chi(k) = \sum_j \frac{N_j S_0^2 F_j(k)}{kR_j^2} exp\left[-2k^2\sigma_j^2\right] exp\left[\frac{-2R_j}{\lambda(k)}\right] sin\left[2k\,R_j + \emptyset_j(k)\right]$$

where S_0^2 is the amplitude reduction factor, $\emptyset F_j(k)$ is the effective curved wave backscattering amplitude, N_j is the number of neighbors in the j^{th} atomic shell, R_j is the distance between the X-ray absorbing central atom and the atoms in the j^{th} atomic shell (backscatterer), λ is the mean free path in Å, $\emptyset F_j(k)$ is the phase shift (including the phase shift for each shell and the total central atom phase shift), σ_j is the Debye Waller parameter of the j^{th} atomic shell (variation of distances around the average R_j).The functions $F_j(k)$, λ and $\emptyset F_j(k)$ were calculated with the ab initio code FEFF6.0.

Synthesis of Ni−NC_3 and Ni−N_4.

Ni−NC_3 and **Ni−N_4** were prepared according to the literature.[3] The as-prepared **MAF−5** or **MAF−4** (200 mg) was heated to 950 °C with a heat rate of 5 °C/min and maintained at this temperature for 3 h in Ar atmosphere to obtain sample A. Sample A (20 mg) and 10 mL ethanol were added into a 20 mL Pyrex vial, and the solution was sonicated for 10 min. Subsequently, 0.3 mL ethanol solution of $Ni(NO_3)_2 \cdot 6H_2O$ (10 mg/mL) was added into the solution of sample A. And the mixture was heated at 80 °C for 5 h, sample B was collected by centrifuging, washed several times with ethanol and dried at 80 °C under vacuum. Then, sample B was heated to 700 °C with a heating rate of 5 °C/min, and maintained at this temperature for 3 h in Ar atmosphere to obtain **Ni−NC_3** or **Ni−N_4**.

CO_2 electroreduction reaction measurements.

All the electrochemical experiments were performed in a flow-cell device (Gaossunion101017) with two-compartments separated by a bipolar membrane (BPM). Electrochemical measurements were performed in a three-electrode cell using the Ag/AgCl electrode as the reference electrode and Pt foil as the counter electrode. Typically, catalyst (10 mg), Nafion (50 μL 5 wt%), ethanol (500 μL) and distilled water (450 μL) were sonicated for 0.5 h. Then the resulting ink (50 μL) was dropped onto Sigracet gas diffusion layer (Fuel Cell store) with a catalyst loading of ~0.3 mg cm^{-2}. The working area is 0.2 cm^{-2}.

Synthesis of Ni-NC_3@Cu_2O-10 and Ni-N_4@Cu_2O-10 working electrodes.

Ni-NC_3@Cu_2O-10 and **Ni-N_4@Cu_2O-10** working electrodes were prepared by a modification of the previous report.[4] In a typical procedure, 7.82 g $CuSO_4 \cdot 5H_2O$ was ultrasonically dissolved in 100 mL H_2O, and then 13.52 g lactic acid was injected into the solution as complexing agent, after that 3 M NaOH was added dropwise to the solution until it's pH was stabilized at 9. The microcrystalline powder of **Ni-NC_3** or **Ni−N_4** was coated on the carbon paper with Nafion binder to prepare the working electrode, utilizing a three-electrode cell configuration, Cu_2O was deposited on **Ni-NC_3** and **Ni−N_4** with 0.2 cm^2 working area under chronoamperometric model at 55 °C at -0.3 V *vs.* Ag/AgCl, respectively. After the deposition, the working electrodes were gently rinsed with water and dried naturally in the air. To facilitate a comparison of partially and fully Cu_2O-encapsulated materials, we prepared **Ni-NC_3@Cu_2O-10** and **Ni-NC_3@Cu_2O-30** under identical conditions as mentioned above, with the deposition times of 10 and 30 minutes, respectively.

During the electrochemical measurements, the electrolyte solution was purged with CO_2 to obtain the CO_2-saturated 1 M KOH solution (pH = 14). A mass flow controller was used to set the CO_2 flow rate at 10 mL/min. The LSV curves were conducted with scan rate of 10 mV/s. All the potentials were reported with respect to the reversible hydrogen electrode (RHE) without internal resistance (iR) compensation and conversed using the formula:

$$E\ (\text{V } vs.\ \text{RHE}) = E\ (\text{V } vs.\ \text{Ag/AgCl}) + 0.196\ \text{V} + 0.059 \times \text{pH}$$

The electrode was applied for constant voltage, the gas products were analyzed by the gas chromatograph (GC) linking to the cathode cell, which was equipped with two flame ionization detectors (FID) and thermal conductivity detector (TCD). Gaseous products generated during the electrocatalysis were detected by a 7890B system.

The Faradaic efficiency of a certain gas product was calculated by the equation:

$$FE = \frac{PV}{T} \times \frac{vzF}{i}$$

in which P, V and T represent the pressure (1 atm), gas flow rate (10 mL min^{-1}) and room temperature, and v (vol%), i, z, and F represent the volume concentration of gas product, current, number of the electron transfer in electrocatalysis, and Faradaic constant (96485 C mol^{-1}), respectively. After the measurements of gas products, anolyte was collected to determine the content of liquid products *via*

^{1}H NMR measurements. Briefly, 100 μL of 6 mM dimethyl sulfoxide (DMSO) aqueous solution as internal standard and 100 μL of deuterated water were added to 500 μL of the above anolyte, and the ratio of peak area between liquid product and DMSO was used as signal intensity to obtain the mass concentration of liquid product. FE of a certain liquid product was calculated by the equation:

$$FE = \frac{mV}{M} \times \frac{nNF}{Q}$$

in which m, V and M represent the mass concentration, volume of anolyte (30 mL) and relative molecular mass of a certain liquid product, and n and Q represent the number of transferred electrons and charge quantity, respectively.

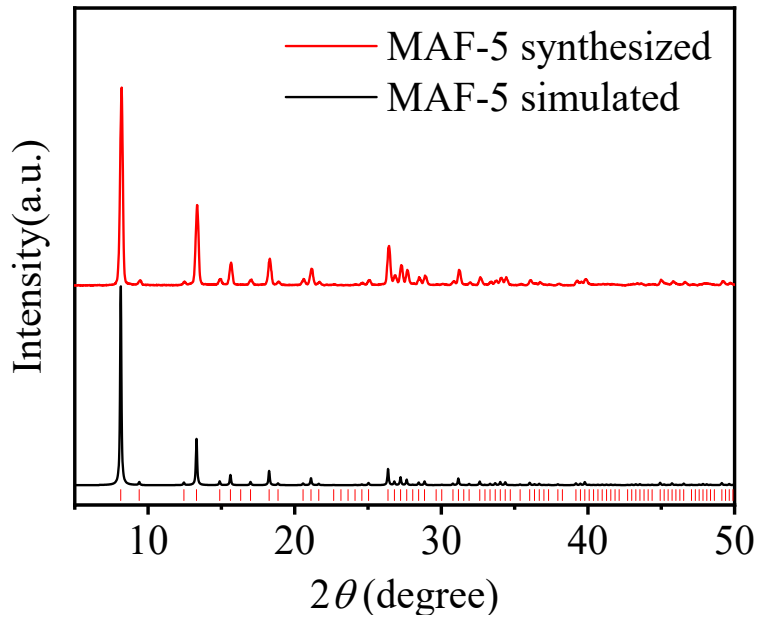

Figure S1. PXRD patterns of **MAF-5**.

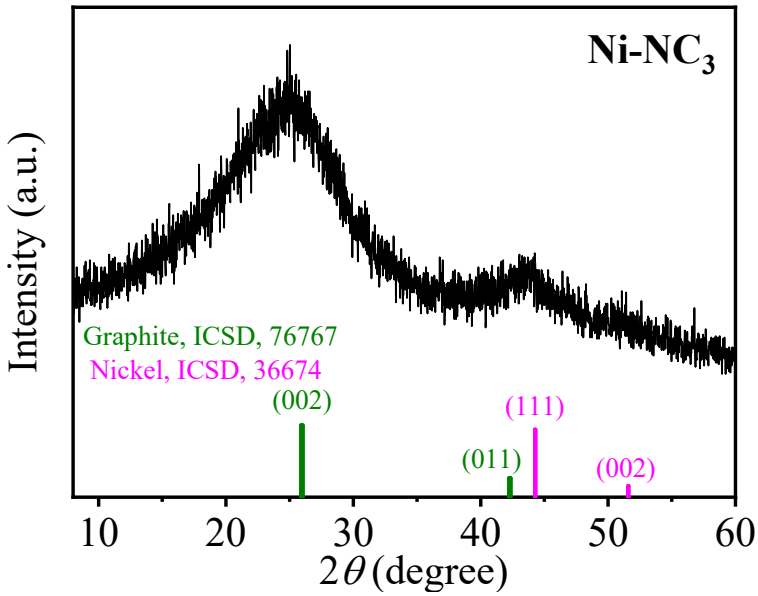

Figure S2. PXRD pattern of **Ni-NC$_3$**.

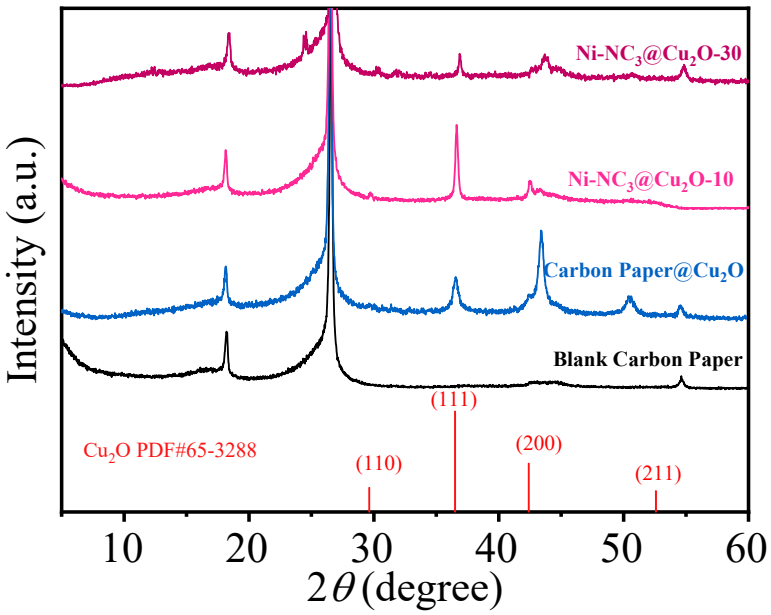

Figure S3. PXRD patterns of **Ni-NC$_3$@Cu$_2$O-30**, **Ni-NC$_3$@Cu$_2$O-10, Carbon Paper@Cu$_2$O** and **Blank Carbon Paper**, respectively.

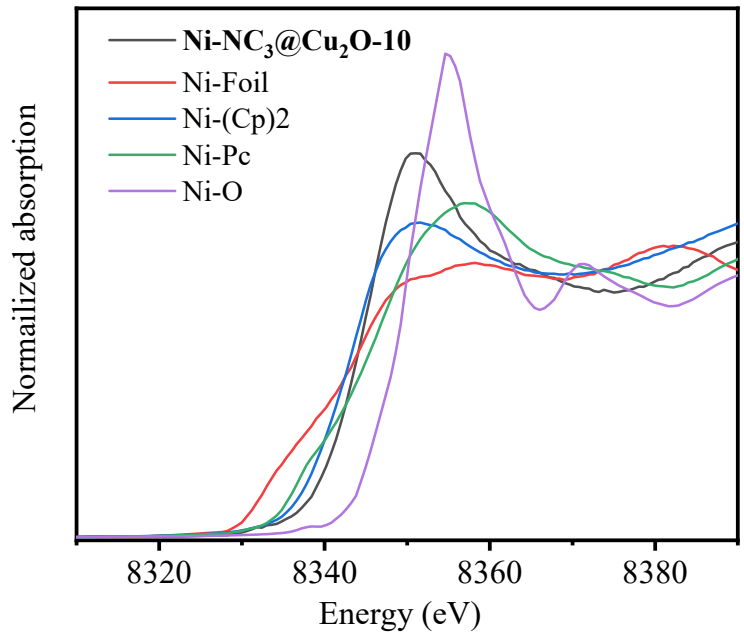

Figure S4. Ni *K*-edge XANES spectra of **Ni-NC$_3$@Cu$_2$O-10** and Ni-based references.

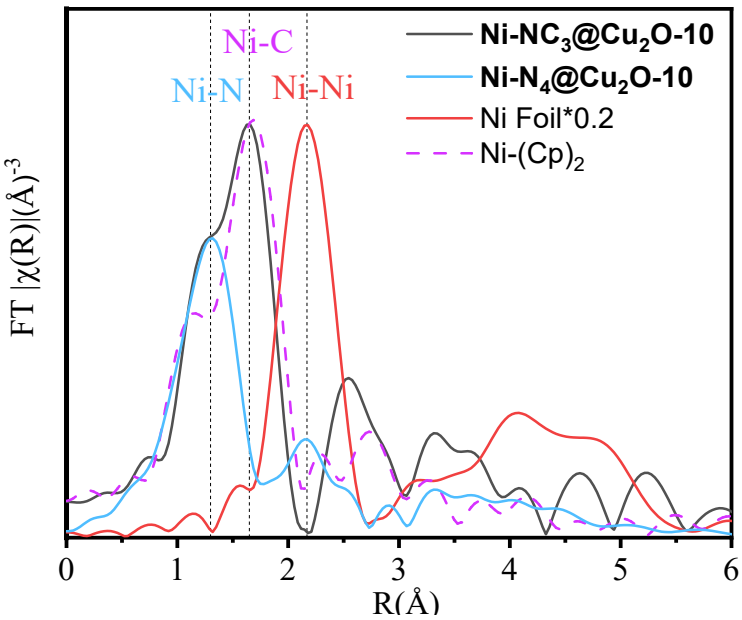

Figure S5. Ni *K*-edge EXAFS spectra of **Ni-NC$_3$@Cu$_2$O-10, Ni-N$_4$@Cu$_2$O-10** and Ni-based references.

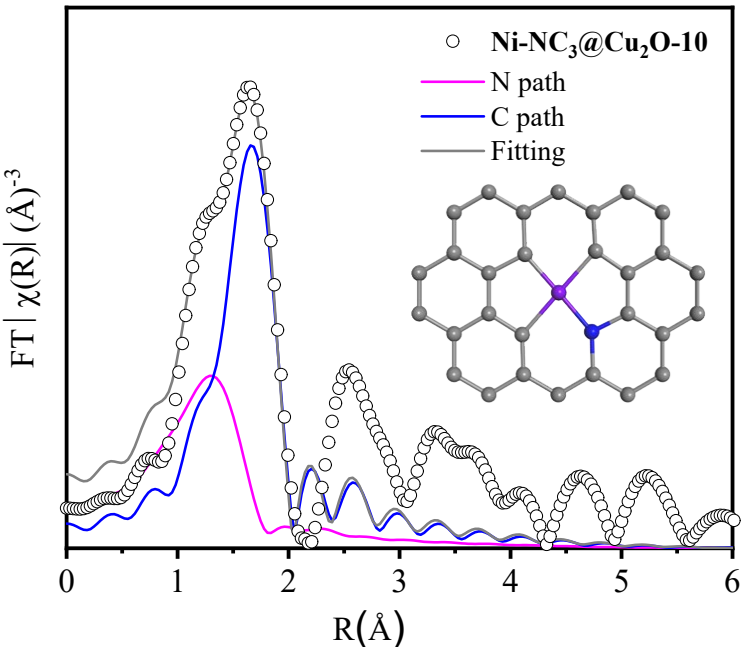

Figure S6. The *R*′ space fitting of the coordination structure of nickel ions in **Ni-NC$_3$**. The inset represents the most likely coordination structure model of the nickel sites in **Ni-NC$_3$**.

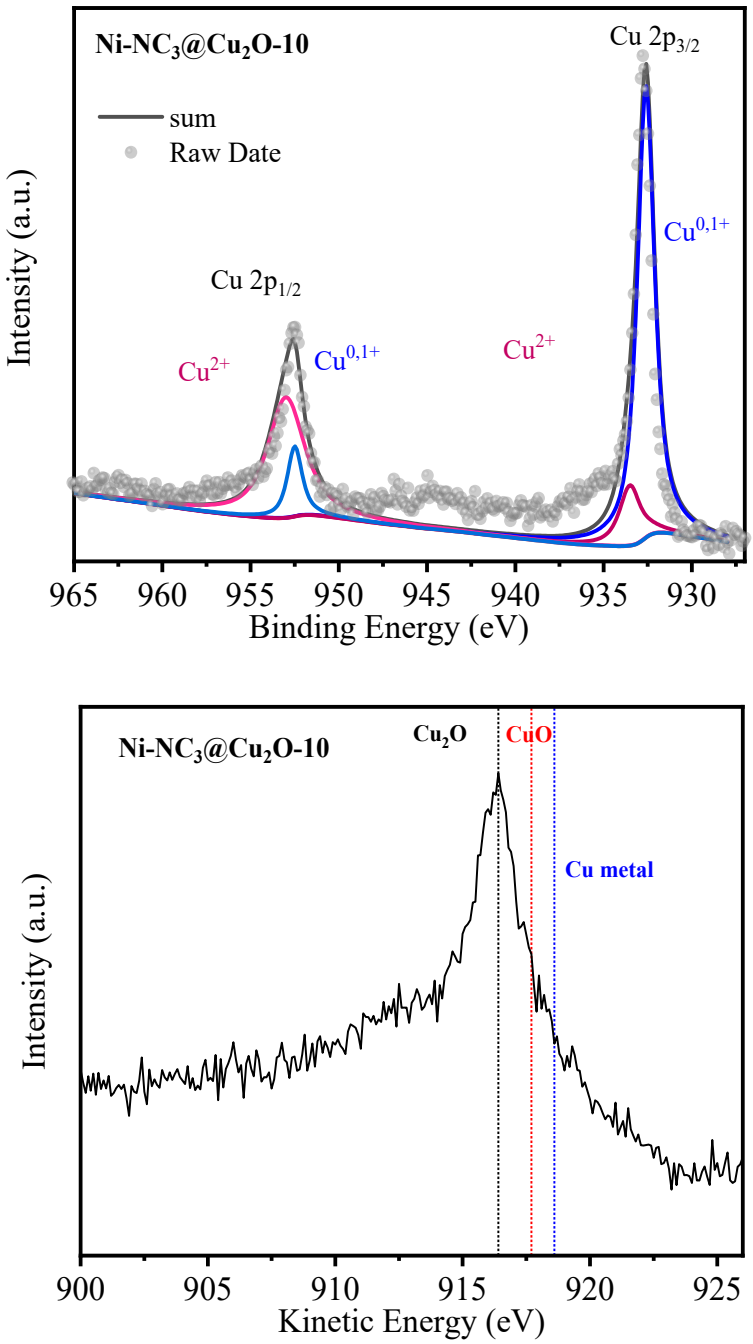

Figure S7. XPS spectra of **Ni-NC$_3$@Cu$_2$O-10**.

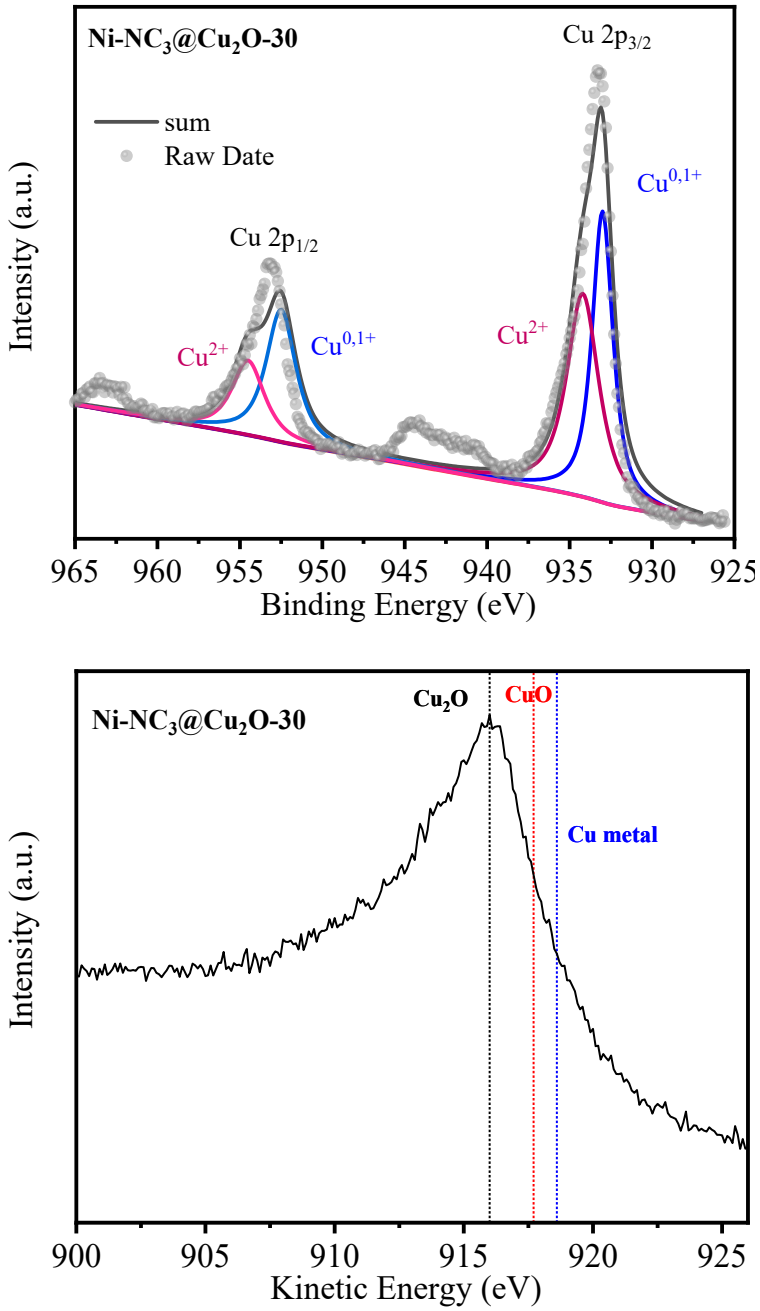

Figure S8. XPS spectra of **Ni-NC$_3$@Cu$_2$O-30**.

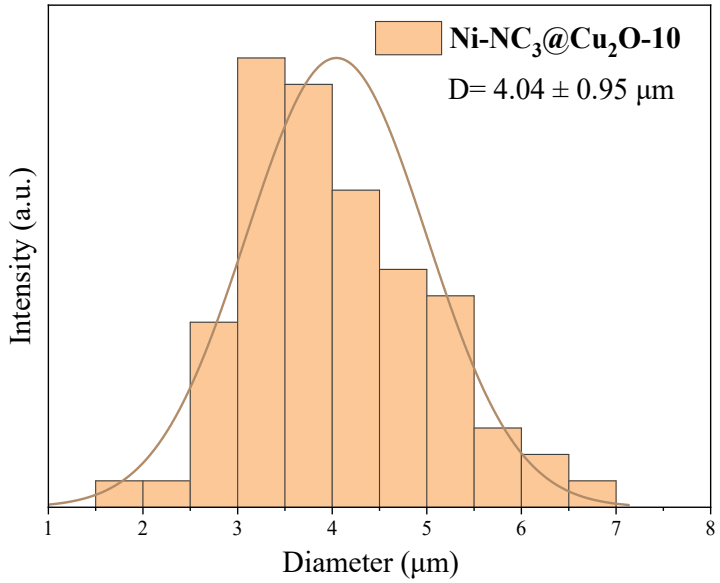

Figure S9. Size distribution of **Ni−NC$_3$@Cu$_2$O-10**.

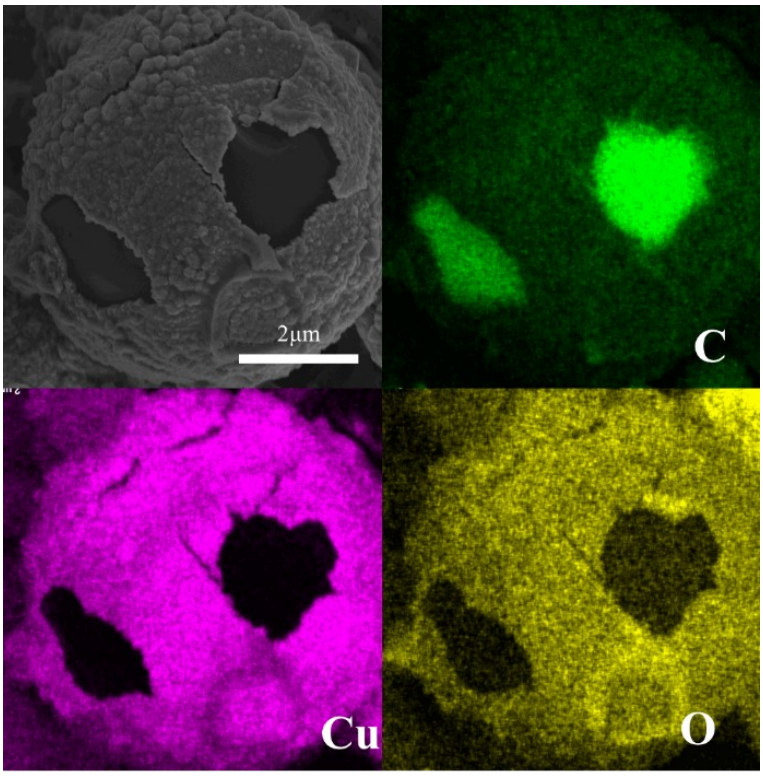

Figure S10. SEM and EDX elemental mapping images of **Ni-NC$_3$@Cu$_2$O-10**.

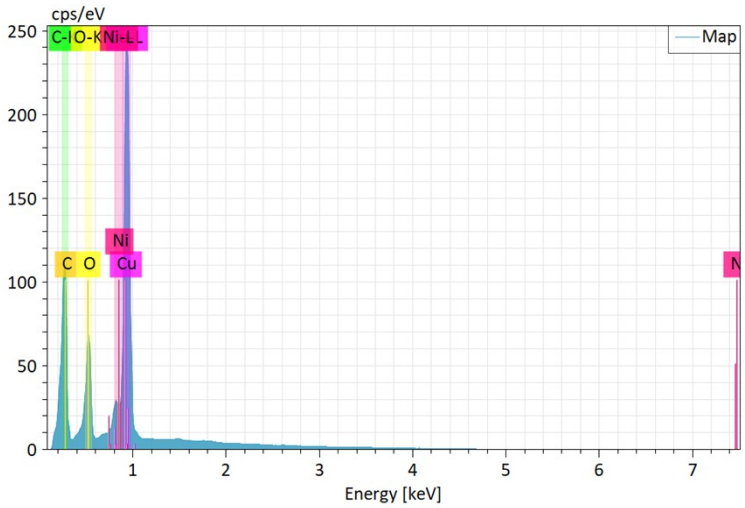

Figure S11. Energy-dispersive X-ray (EDX) spectrum of **Ni−NC$_3$@Cu$_2$O-10**.

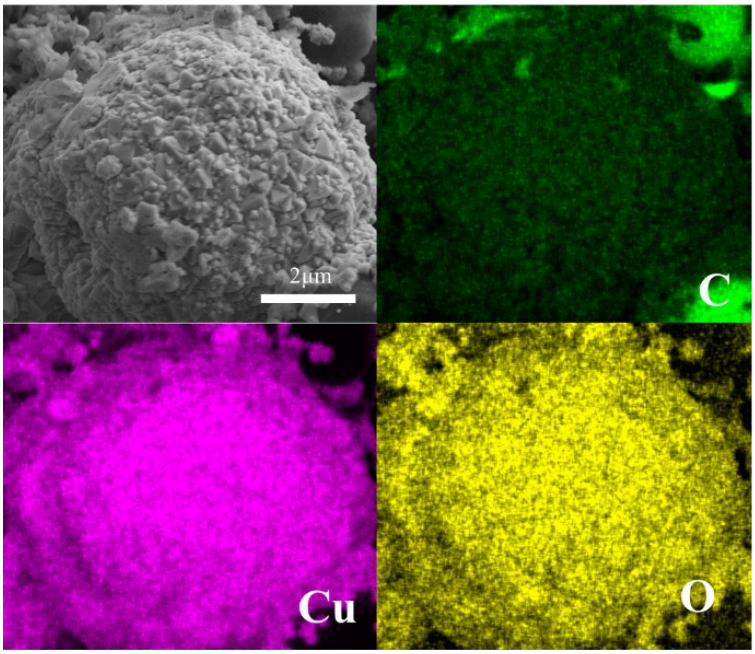

Figure S12. SEM and EDX elemental mapping images of **Ni-NC$_3$@Cu$_2$O-30.**

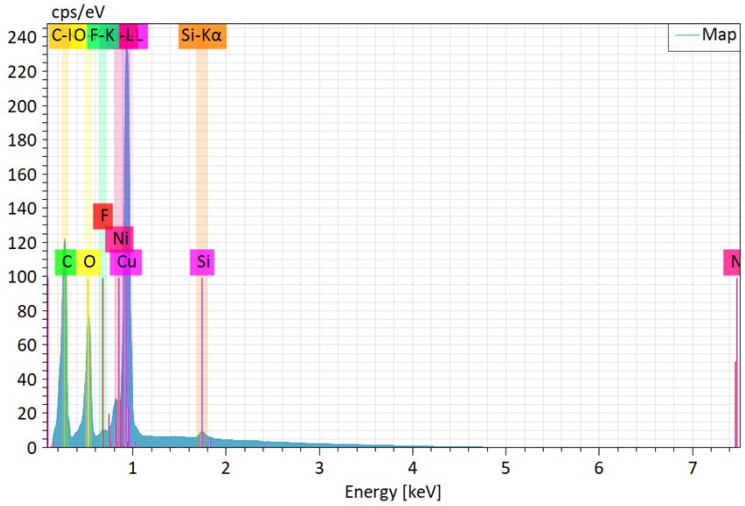

Figure S13. Energy-dispersive X-ray (EDX) spectrum of **Ni−NC$_3$@Cu$_2$O-30**.

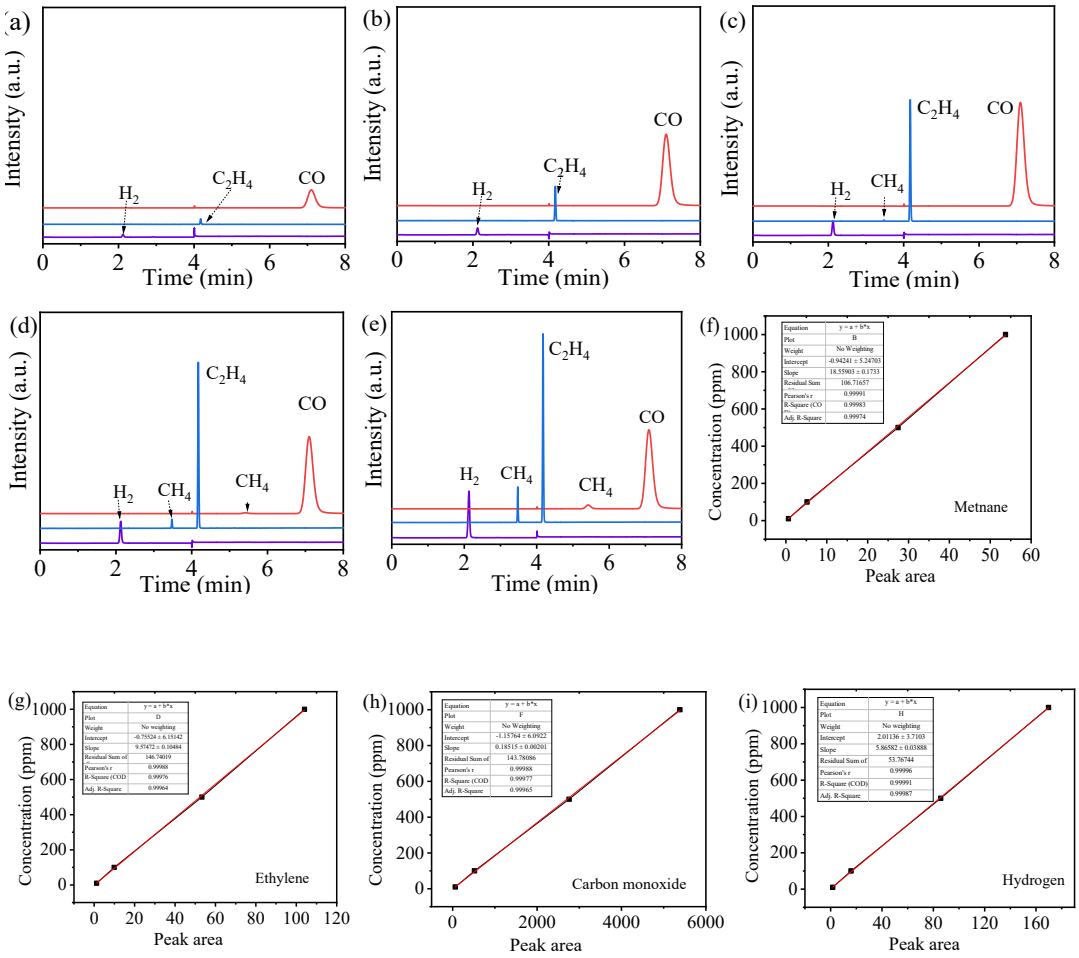

Figure S14. GC profiles of gas products of **Ni−NC$_3$@Cu$_2$O-10** at (a) −0.6 V *vs.* RHE, (b) −0.8 V *vs.* RHE, (c) −1.0 V *vs.* RHE, (d) −1.2 V *vs.* RHE and (e) −1.4 V *vs.* RHE. The calibration curves for (f) methane, (g) ethylene, (h) carbon monoxide, and (i) hydrogen.

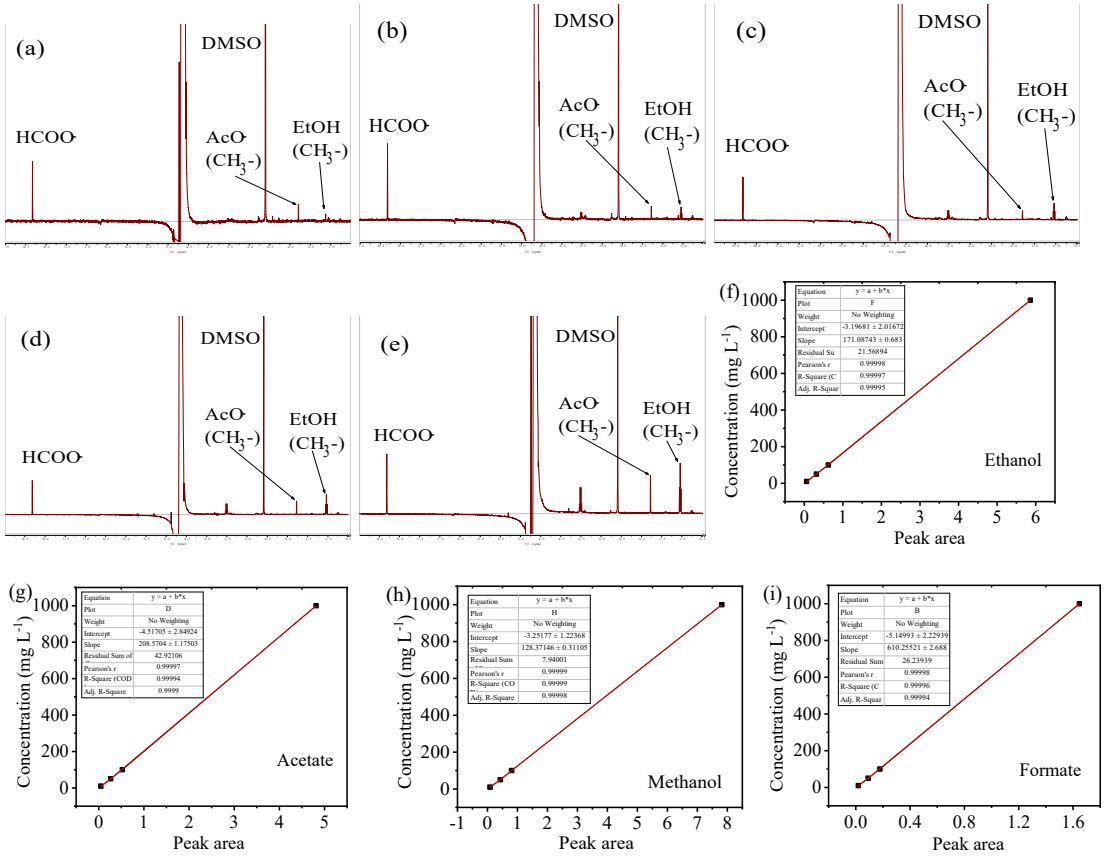

Figure S15. ^{1}H NMR spectra of the liquid products by using **Ni−NC$_3$@Cu$_2$O-10** as catalyst at the potentials of (a) −0.6 V *vs.* RHE, (b) −0.8 V *vs.* RHE, (c) −1.0 V *vs.* RHE, (d) −1.2 V *vs.* RHE and (e) −1.4 V *vs.* RHE. The calibration curves for (f) Ethanol, (g) Acetate, (h) Methanol and (i) Formate.

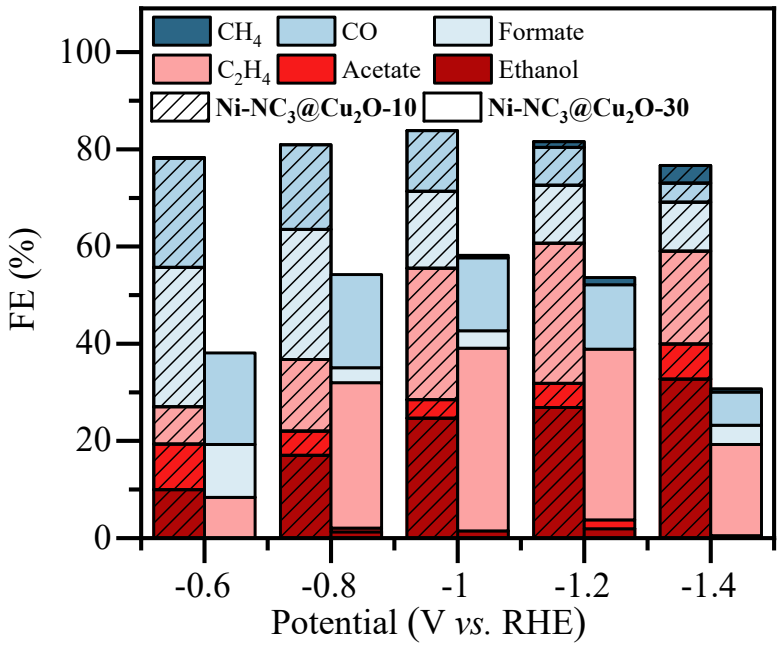

Figure S16. FE values of reduced products by **Ni-NC$_3$@Cu$_2$O-10** and **Ni-NC$_3$@Cu$_2$O-30**, respectively, in CO_2-saturated 1 M KOH solution.

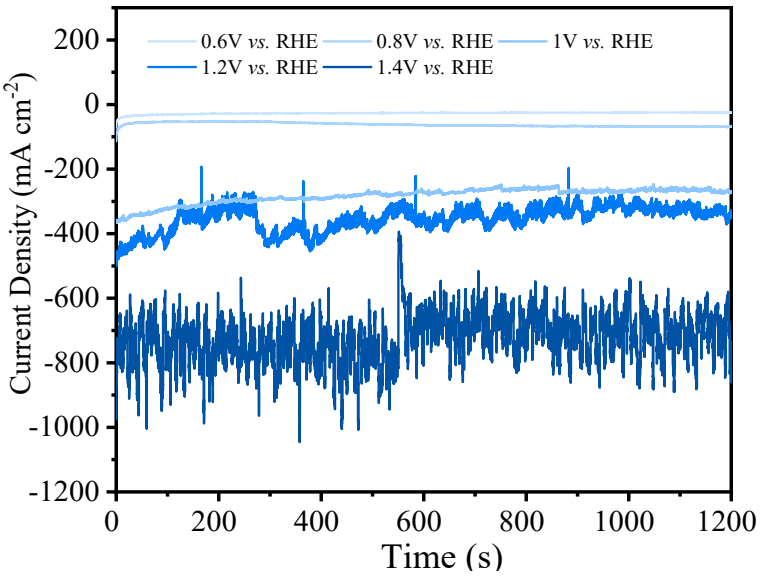

Figure S17. *i-t* curves by **Ni-NC$_3$@Cu$_2$O-10** at different potentials.

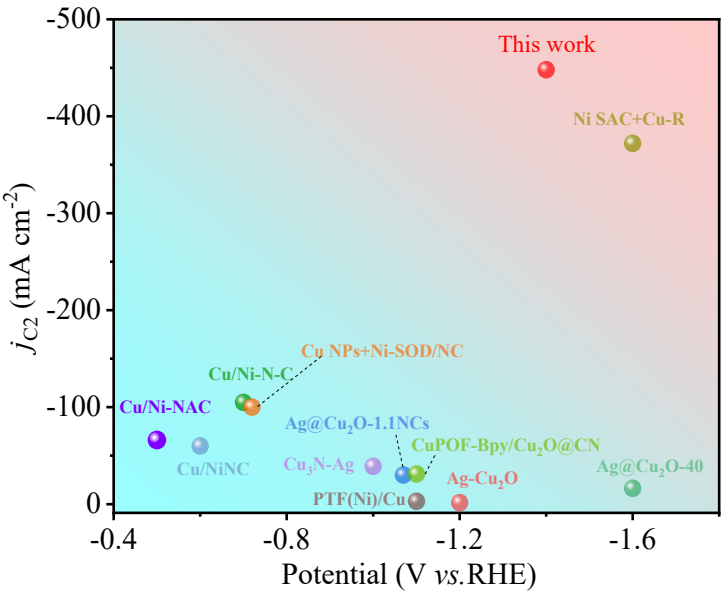

Figure S18. Performance comparison of reported copper-based tandem catalysts for eCO_2RR to C_2 products.

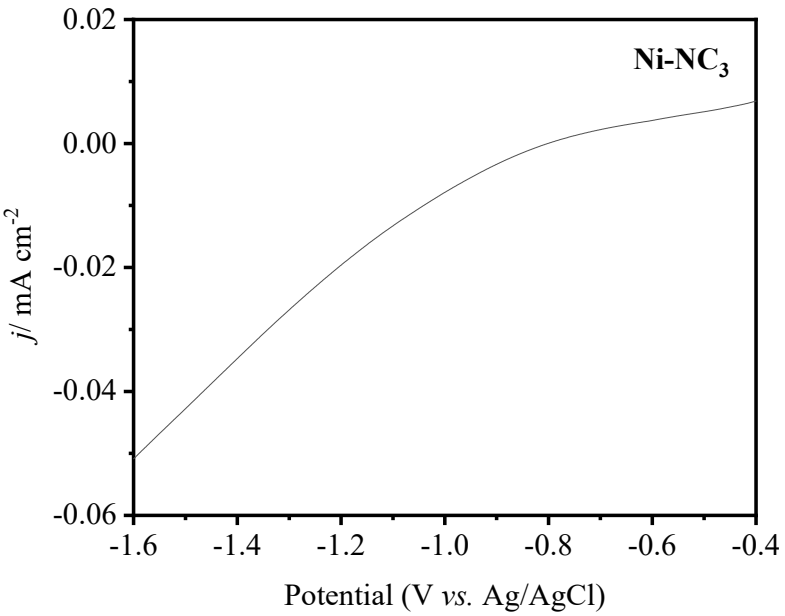

Figure S19. Anodic stripping voltammograms obtained from Carbon Paper electrodes when the potential was held at 1.4 V in a CO_2-saturated 1 M KOH aqueous solution using **Ni-NC$_3$**.

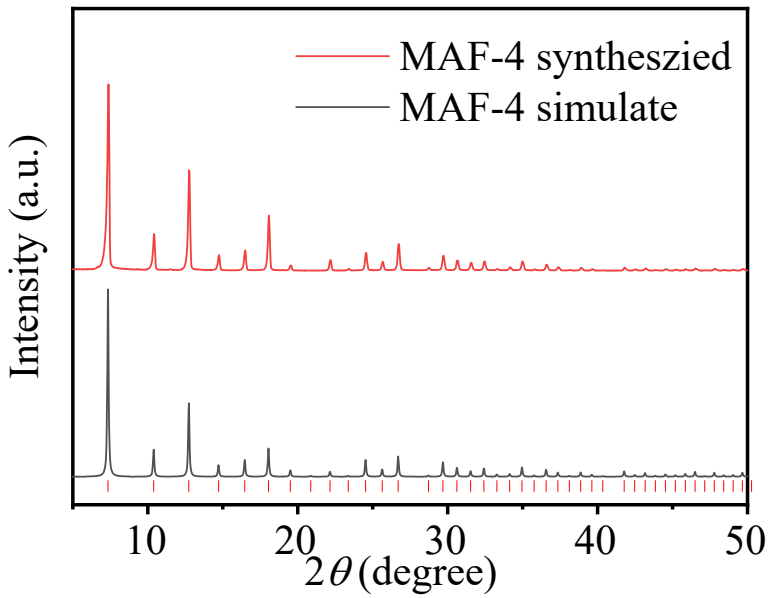

Figure S20. PXRD patterns of **MAF-4**.

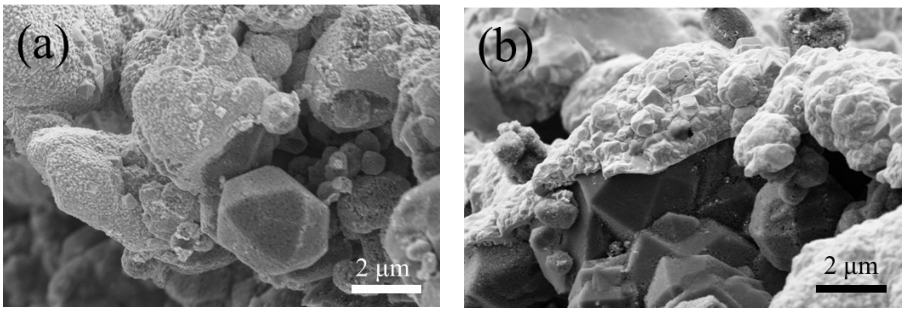

Figure S21. SEM images of (a) **Ni-N_4@Cu_2O-10** and (b) **CB@Cu_2O-10**.

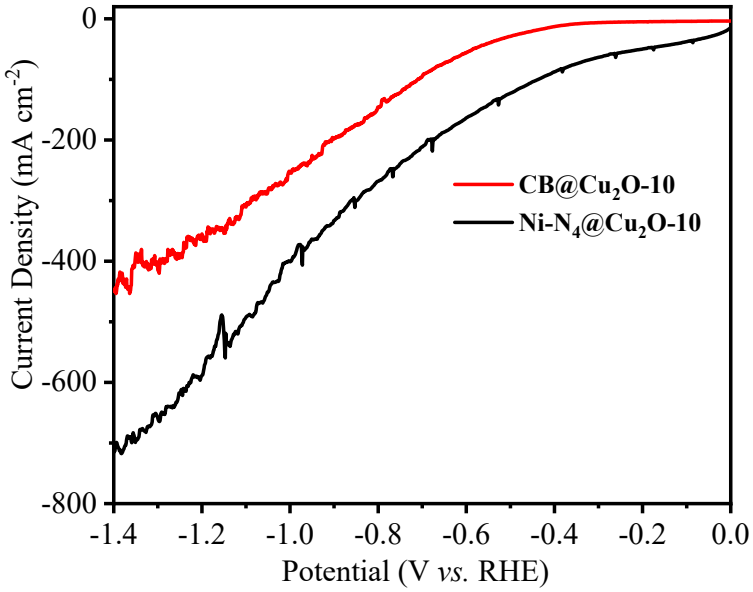

Figure S22. LSV curves by **CB@Cu_2O-10** and **Ni-N_4@Cu_2O-10**, respectively, in CO_2-saturated 1 M KOH solution.

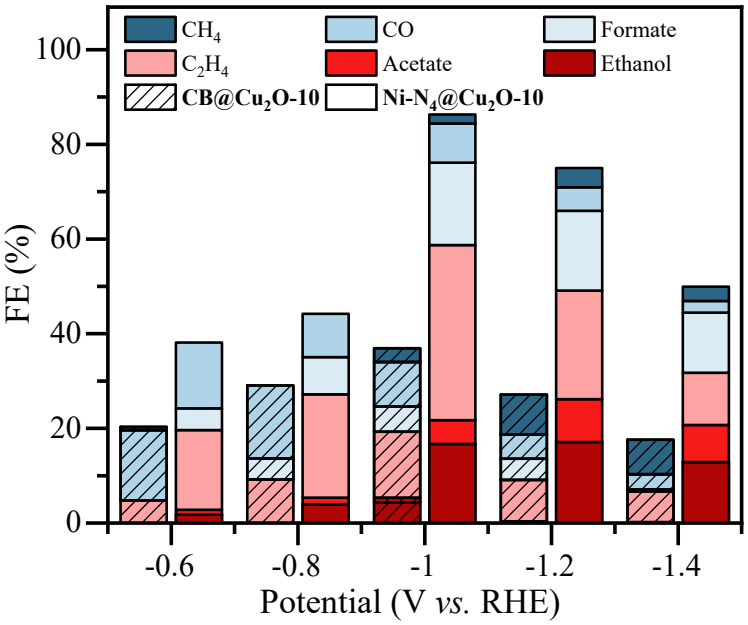

Figure S23. FE values of reduced products by **CB@Cu_2O-10** and **Ni-N_4@Cu_2O-10**, respectively, in CO_2-saturated 1 M KOH solution.

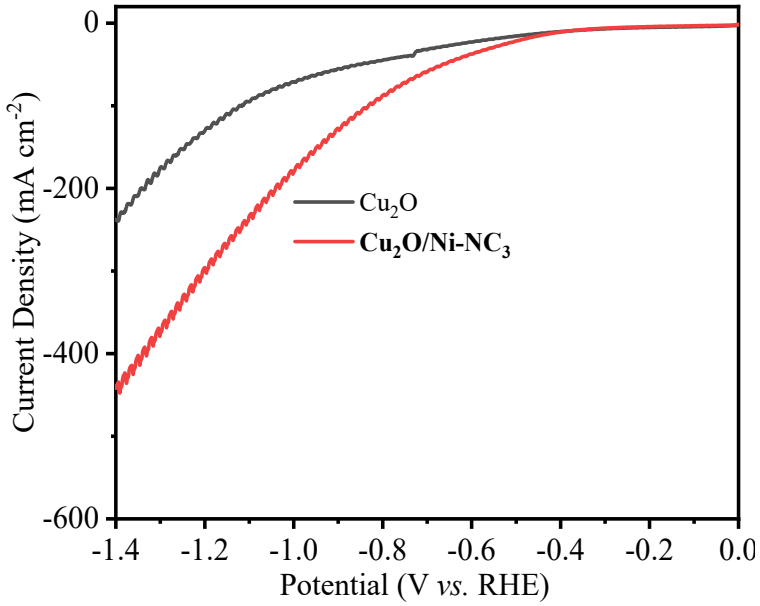

Figure S24. LSV curves by **Cu_2O** and **Cu_2O/Ni-NC_3**, respectively, in CO_2-saturated 1 M KOH solution.

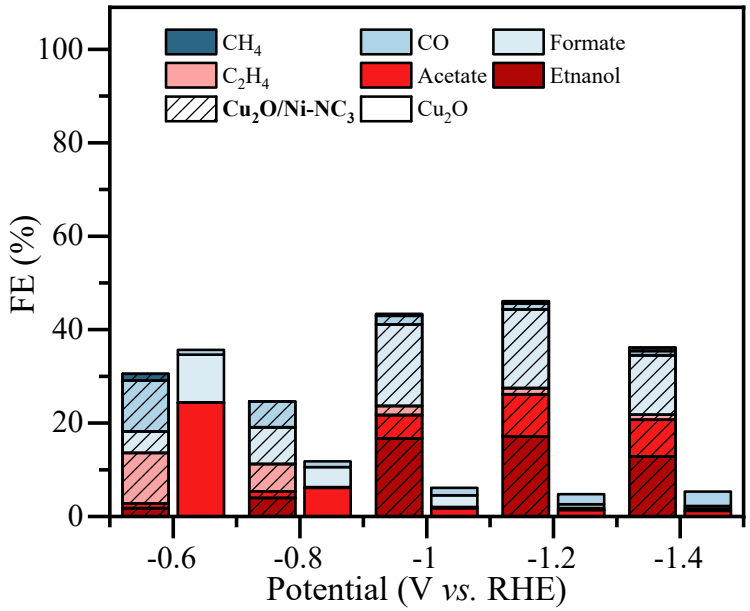

Figure S25. FE values of reduced products by **Cu_2O** and **Cu_2O/Ni-NC_3**, respectively, in CO_2-saturated 1 M KOH solution.

Table S1. Summary of the fitting parameters for Cu and Ni *K*-edge EXAFS curves.

Sample	Shell	CN	*R* (Å)	$\sigma^2(10^{-3}Å^2)$	$\Delta E_0(eV)$	*R*-factor
Ni–NC$_3$@Cu$_2$O-10	Cu-O	4	1.44	5.4	-4.31	0.019
	Ni-N	1	1.91	4.9	-4.7	0.018
	Ni-C	3	2.08	5.2	-9.6	

CN, coordination number; σ^2, Debye-Waller factor to describe the variance in due to disorder (both lattice and thermal) (σ^2 typically has a value of 0.003 ~ 0.02); ΔE_0, threshold Energy Correction ($|\Delta E_0|$ typically has a value of < 10). *R*-factor is used to evaluate the quality of the fitting and the smaller value means better fitting result (*R*-factor typically has a value of < 0.02). The fit of Ni−N was performed by fixing the S_0^2 value to 0.85, which was obtained from the experimental EXAFS fit of Ni reference by fixing CN as the known crystallographic value.

It should be noted that the fitting bond-length does not exactly correspond to the EXAFS fitting curve at *R*-space. This is because Fourier transformed k^2-weighted EXAFS cancels out the phase shift and is only used for qualitative analysis. Even when phase correction is considered, it is imprecise and does not completely correlate with the fitting bond-length.

Table S2. Element compositions of **Ni-NC$_3$@Cu$_2$O-10**.

Element	Mass Norm. (%)	Atom (%)	Abs. error (%)
C	10.46	30.65	0.37
O	11.95	26.29	0.34
Ni	1.43	0.86	0.06
Cu	76.17	42.20	1.95

Table S3. Element compositions of **Ni-NC$_3$@Cu$_2$O-30**.

Element	Mass Norm. (%)	Atom (%)	Abs. error (%)
C	11.12	30.85	0.39
O	13.04	27.16	0.37
Ni	1.43	0.81	0.06
Cu	72.24	37.89	1.86

Table S4. Performance comparison of various reported copper-based tandem catalysts for eCO$_2$RR to C$_2$ products.

Catalyst	FE_{C2}%	Potential V *vs.* RHE	j_{C2} mA cm^{-2}	Stability (h)	Electrolyte	Ref.
Ni-NC$_3$@Cu$_2$O-10	61	-1.4	-448	32	1 M KOH	This work
Ag-Cu$_2$O	49	-1.2	-1.5	3	0.2 M KCl	5
Ag@Cu$_2$O-1.1 NCs	30	-1.1	-30	5.5	0.1 M KHCO$_3$	6
Ag@Cu$_2$O-40	78	-1.6	-16.4	6	0.1 M KHCO$_3$	7
Cu$_3$N-Ag	54	-1.0	-39	1	1 M KOH	8
Cu/Ni-NAC	66	-0.5	-66	10	1 M KOH	9
Cu/Ni-N-C	70	-0.7	-105	100	1 M KOH	10
PTF(Ni)/Cu	57.8	-1.1	-3	12	0.1 M KCl / 0.1 M KHCO$_3$	11
Ni SAC+Cu-R	62	-1.6	-372	14	1 M KHCO$_3$	12
Cu NPs+Ni-SOD/NC	62	-0.72	-100	16	0.5 M KHCO$_3$	13
Cu/NiNC	40	-0.6	60	1	1 M KHCO$_3$	14
CuPOF-Bpy/ Cu$_2$O@CN	71	-1.1	-31	0.3	0.5 M KHCO$_3$	15

Table S5. ICP results of the electrolyte of **Ni-NC$_3$** and **Ni-NC$_3$@Cu$_2$O-10** after catalysis.

Catalyst	Ni	Cu
Ni–NC$_3$	-	
Ni–NC$_3$@Cu$_2$O-10	-	-

The detection limit for Ni is 0.02 mg/L, and for Cu is 0.01 mg/L, "-" indicates not detected.

The electrolyte was collected following 30 minutes of electrocatalysis at -1.4 V versus RHE. 0.1 mL of the electrolyte was extracted and neutralized to pH = 7 with 1 M HNO_3 aqueous solution.

Considering the measurement range of ICP-AES, it was subsequently diluted to 10 mL with a 5 wt% HNO_3 aqueous solution for detection. No Ni or Cu elements were identified in the aforesaid electrolyte.

References

1. X. C. Huang, Y. Y. Lin, J. P. Zhang and X. M. Chen, Ligand‐Directed Strategy for Zeolite‐Type Metal‐Organic Frameworks: Zinc(II) Imidazolates with Unusual Zeolitic Topologies, *Angew. Chem. Int. Ed.*, 2006, **45**, 1557-1559.
2. A.-X. Zhu, R.-B. Lin, X.-L. Qi, Y. Liu, Y.-Y. Lin, J.-P. Zhang and X.-M. Chen, Zeolitic metal azolate frameworks (MAFs) from ZnO/$Zn(OH)_2$ and monoalkyl-substituted imidazoles and 1,2,4-triazoles: Efficient syntheses and properties, *Microporous and Mesoporous Materials*, 2012, **157**, 42-49.
3. C.-P. Liang, J.-R. Huang, H.-L. Zhu, Z.-H. Zhao, C. Yu, P.-Q. Liao and X.-M. Chen, Precisely Tailoring the First Coordination Shell of Metal Centers in Porous Nitrogen‐Doped Carbon Promoting Electroreduction of CO_2 Under Neutral Condition, *CCS Chem.*, 2024, **6**, 1978-1986.
4. L. Chen, J. Chen, L. Fan, J. Chen, T. Zhang, J. Chen, S. Xi, B. Chen and L. Wang, Additive‐Assisted Electrodeposition of Cu on Gas Diffusion Electrodes Enables Selective CO_2 Reduction to Multicarbon Products, *ACS Catal.*, 2023, **13**, 11934-11944.
5. S. Lee, G. Park and J. Lee, Importance of Ag‐Cu Biphasic Boundaries for Selective Electrochemical Reduction of CO_2 to Ethanol, *ACS Catal.*, 2017, **7**, 8594-8604.
6. L. Xiong, X. Zhang, L. Chen, Z. Deng, S. Han, Y. Chen, J. Zhong, H. Sun, Y. Lian, B. Yang, X. Yuan, H. Yu, Y. Liu, X. Yang, J. Guo, M. H. Rümmeli, Y. Jiao and Y. Peng, Geometric Modulation of Local CO Flux in Ag@Cu_2O Nanoreactors for Steering the CO_2RR Pathway toward High‐Efficacy Methane Production, *Adv. Mater.*, 2021, **33**, 2101741.
7. Y. Lu, H. Li, H. Sun, J. Zhao, Y. Zhang, Y. Wang, C. Zhu, D. Gao, Y. Tuo, J. Zeng, D. Chen and Z. Yan, Confinement Catalysis of Reaction Intermediates in Ag@Cu_2O Cascade Nanoreactors toward Boosted Electrochemical C‐C Coupling, *ACS Catal.*, 2024, **14**, 14744-14753.
8. J. Li, Y. Chen, B. Yao, W. Yang, X. Cui, H. Liu, S. Dai, S. Xi, Z. Sun, W. Chen, Y. Qin, J. Wang, Q. He, C. Ling, D. Wang and Z. Zhang, Cascade Dual Sites Modulate Local CO Coverage and Hydrogen‐Binding Strength to Boost CO_2 Electroreduction to Ethylene, *J. Am. Chem. Soc.*, 2024, **146**, 5693-5701.
9. Z. Yin, J. Yu, Z. Xie, S.-W. Yu, L. Zhang, T. Akauola, J. G. Chen, W. Huang, L. Qi and S. Zhang, Hybrid Catalyst Coupling Single‐Atom Ni and Nanoscale Cu for Efficient CO_2 Electroreduction to Ethylene, *J. Am. Chem. Soc.*, 2022, **144**, 20931-20938.
10. X. She, T. Zhang, Z. Li, H. Li, H. Xu and J. Wu, Tandem Electrodes for Carbon Dioxide

Reduction into C_{2+} Products at Simultaneously High Production Efficiency and Rate, *Cell Rep. Phys. Sci.*, 2020, **1**, 100051.

11. D. L. Meng, M. D. Zhang, D. H. Si, M. J. Mao, Y. Hou, Y. B. Huang and R. Cao, Highly Selective Tandem Electroreduction of CO_2 to Ethylene over Atomically Isolated Nickel‐Nitrogen Site/Copper Nanoparticle Catalysts, *Angew. Chem. Int. Ed.*, 2021, **60**, 25485-25492.
12. M. Liu, Q. Wang, T. Luo, M. Herran, X. Cao, W. Liao, L. Zhu, H. Li, A. Stefancu, Y.-R. Lu, T.-S. Chan, E. Pensa, C. Ma, S. Zhang, R. Xiao and E. Cortés, Potential Alignment in Tandem Catalysts Enhances CO_2‐to‐C_2H_4 Conversion Efficiencies, *J. Am. Chem. Soc.*, 2023, **146**, 468-475.
13. J. Chen, D. Wang, X. Yang, W. Cui, X. Sang, Z. Zhao, L. Wang, Z. Li, B. Yang, L. Lei, J. Zheng, L. Dai and Y. Hou, Accelerated Transfer and Spillover of Carbon Monoxide through Tandem Catalysis for Kinetics‐boosted Ethylene Electrosynthesis, *Angew. Chem. Int. Ed.*, 2023, **62**, e202215406.
14. Y. R. Lin, D. U. Lee, S. Tan, D. M. Koshy, T. Y. Lin, L. Wang, D. Corral, J. E. Avilés Acosta, J. A. Zamora Zeledon, V. A. Beck, S. E. Baker, E. B. Duoss, C. Hahn and T. F. Jaramillo, Vapor‐Fed Electrolyzers for Carbon Dioxide Reduction Using Tandem Electrocatalysts: Cuprous Oxide Coupled with Nickel‐Coordinated Nitrogen‐Doped Carbon, *Adv. Funct. Mater.*, 2022, **32**, 2113252.
15. Q. He, H. Li, Z. Hu, L. Lei, D. Wang and T. T. Li, Highly Selective CO_2 Electroreduction to C_2H_4 Using a Dual‐Sites Cu(II) Porphyrin Framework Coupled with Cu_2O Nanoparticles via a Synergetic‐Tandem Strategy, *Angew. Chem. Int. Ed.*, 2024, **63**, e202407090.